Systems/Circuits

# Specialized Pathways from the Primate Amygdala to Posterior Orbitofrontal Cortex

**Clare Timbie**[1] **and Helen Barbas**[1,2]
[1]Department of Anatomy and Neurobiology, Boston University School of Medicine, Boston, Massachusetts 02118, and [2]Department of Health Sciences, Boston University, Boston, Massachusetts 02215

The primate amygdala sends dense projections to posterior orbitofrontal cortex (pOFC) in pathways that are critical for processing emotional content, but the synaptic mechanisms are not understood. We addressed this issue by investigating pathways in rhesus monkeys (*Macaca mulatta*) from the amygdala to pOFC at the level of the system and synapse. Terminations from the amygdala were denser and larger in pOFC compared with the anterior cingulate cortex, which is also strongly connected with the amygdala. Axons from the amygdala terminated most densely in the upper layers of pOFC through large terminals. Most of these terminals innervated spines of presumed excitatory neurons and many were frequently multisynaptic and perforated, suggesting high synaptic efficacy. These amygdalar synapses in pOFC exceeded in size and specialization even thalamocortical terminals from the prefrontal-related thalamic mediodorsal nucleus to the middle cortical layers, which are thought to be highly efficient drivers of cortical neurons. Pathway terminals in the upper layers impinge on the apical dendrites of neurons in other layers, suggesting that the robust amygdalar projections may also activate neurons in layer 5 that project back to the amygdala and beyond to autonomic structures. Among inhibitory neurons, the amygdalar pathway innervated preferentially the neurochemical classes of calbindin and calretinin neurons in the upper layers of pOFC, which are synaptically suited to suppress noise and enhance signals. These features provide a circuit mechanism for flexibly shifting focus and adjusting emotional drive in processes disrupted in psychiatric disorders, such as phobias and obsessive– compulsive disorder.

*Key words:* emotion and amygdala; neural circuits; OCD; orbitofrontal; synapse; thalamus

## Introduction

Emotions guide decisions and their disruption impairs flexible behavior as in obsessive–compulsive disorder and autism (Bachevalier and Loveland, 2006; Maia et al., 2008). The amygdala has been implicated in emotional processes and, through connections with prefrontal cortex (Porrino et al., 1981; Ghashghaei and Barbas, 2002), likely transmits affective valence that influences executive functions (for review, see Bechara et al., 2000; Murray, 2007).

Pathways from the amygdala terminate most densely in posterior orbitofrontal cortex (pOFC) and anterior cingulate cortex (ACC; Ghashghaei et al., 2007). The pOFC also receives input representing all sensory modalities from high-order sensory association cortices (for review, see Cavada et al., 2000; Barbas et al.,

2011). As the most multimodal prefrontal region and biased recipient of amygdalar pathways, the pOFC is poised to integrate signals from the external environment and the internal milieu associated with the affective significance of stimuli. In contrast, the ACC is a biased sender of projections to the amygdala (Ghashghaei et al., 2007), mediating emotional expression through pathways to central autonomic structures (for review, see Devinsky et al., 1995).

Another strong pathway to pOFC is from the mediodorsal thalamic nucleus (MD) and adjacent midline nuclei (Goldman-Rakic and Porrino, 1985; Dermon and Barbas, 1994). The amygdalar and thalamic pathways show opposite laminar innervation in pOFC (Porrino et al., 1981). Amygdalar fibers densely innervate lower layer 1 and layer 2 and to a lesser extent all other layers (Ghashghaei et al., 2007), while MD innervates most densely the middle cortical layers and to a lesser extent the upper layers (McFarland and Haber, 2002). Different layers represent distinct microenvironments. The upper layers (1–3a) include dendrites from pyramidal neurons in layers 2–5 (DeFelipe and Farinas, 1992) and among inhibitory neurons they are populated preferentially with the neurochemical classes of calretinin (CR) and calbindin (CB) neurons. In contrast, the middle layers are preferentially populated with parvalbumin (PV) inhibitory neurons (Gabbott and Bacon, 1996; Dombrowski et al., 2001).

Pathways that terminate in different layers are thought to differ functionally. Sensory thalamic pathways to the middle cortical layers have been called "drivers" because they reliably elicit action

**Table 1. Injection sites in amygdalar and thalamic nuclei**

| Case; hemisphere | Injection site; division | Tracer | Sex | Age (years) |
|---|---|---|---|---|
| BB; left (BB-L) | Amygdala; basomedial, basolateral, anterior | BDA | Female | 2 |
| BB; right (BB-R) | Amygdala; basolateral, anterior, basomedial, cortical | BDA | Female | 2 |
| BD; left (BD-L) | Amygdala; basolateral, central, lateral, basomedial | BDA | Male | 2 |
| BD; right (BD-R) | Amygdala; cortical, medial, basomedial, basolateral | BDA | Male | 2 |
| BL; right (BL-R) | Amygdala; cortical, basomedial | FR | Male | 3 |
| BM; right (BM-R) | Amygdala; basomedial, cortical | FR | Female | 3.5 |
| BN; right (BN-R) | Amygdala; basomedial, basolateral | FE | Male | 2 |
| BB; left (BB-L) | Thalamus; mediodorsal magnocellular, mediodorsal parvicellular | FE | Female | 2 |
| BO; right (BO-R) | Thalamus; mediodorsal magnocellular, paraventricular, central intermediate | LY | Male | 3 |
| BN; right (BN-R) | Thalamus; mediodorsal parvicellular, habenula | CBL | Male | 2 |

potentials in postsynaptic neurons, assuring transmission of signals (Sherman and Guillery, 1998). Pathways that terminate in the upper layers form synapses distally on postsynaptic neurons, mildly change their excitability, and thus have been called "modulators" (Sherman and Guillery, 1998). While the predominant termination pattern of amygdalar fibers in upper pOFC layers suggests a modulatory role, there is evidence that the amygdala can drive cortical neurons, at least in mice (Little and Carter, 2013).

Understanding the features of pathways from the amygdala to distinct prefrontal cortices in comparison with parallel thalamocortical pathways is prerequisite to unraveling core cognitive–emotional interactions that are disrupted in psychiatric disorders. Key outstanding questions addressed in this study pertain to the strength and potential efficacy of these pathways and interactions with excitatory and distinct classes of inhibitory neurons in prefrontal cortices. We identified specializations in amygdalar pathways to pOFC, suggesting specificity in the information conveyed by this strong pathway for flexible behavior.

## Materials and Methods

### Surgery, tracer injections, and tissue processing

Experiments were conducted on six rhesus monkeys (*Macaca mulatta*) aged 2–3.5 years of both sexes injected with 1–2 distinct neural tracers for 10 cases overall (Table 1). Experiments were conducted according to the *Guide for the Care and Use of Laboratory Animals* (National Research Council, 2011). Experimental methods were approved by the institutional animal care and use committees at Boston University School of Medicine, Harvard Medical School, and New England Primate Research Center. Procedures involving animals were designed to reduce the number of animals needed and minimize animal suffering.

To calculate stereotaxic coordinates for the injection sites, magnetic resonance images were obtained before surgery following animal sedation with ketamine hydrochloride and propofol anesthesia. Experiments were conducted under sterile conditions, and animals were continuously monitored for respiratory rate, oxygen saturation, heart rate, and temperature. For surgery, the animals were placed under isoflurane anesthesia and positioned in stereotaxic apparatus (Kopf 1430M, David Kopf Instruments), and a small opening was made in the skull and dura. We injected 10% dilutions of Lucifer yellow dextran (LY, 4 $\mu$l, 10 kDa; Invitrogen), fluoroemerald (FE, fluorescein dextran, 3 $\mu$l, 10 kDa or a mixture of 3 kDa and 10 kDa; Invitrogen), fluororuby (FR, tetramethylrhodamine dextran, 3–4 $\mu$l, mixture of 3 kDa and 10 kDa; Invitrogen), biotinylated dextran amine (BDA, 9 $\mu$l, 3 kDa or a mixture of 3 kDa and 10 kDa; Invitrogen), or cascade blue dextran (CBL, 6 $\mu$l, mixture of 3 kDa and 10 kDa; Invitrogen) into amygdalar or thalamic nuclei using Hamilton syringes (10 $\mu$l). After 18 d, the animals were anesthetized with sodium pentobarbital and perfused transcardially with 4% paraformaldehyde, 0.2% glutaraldehyde in 0.1 M phosphate buffer saline (PBS), pH 7.4. The brain was removed, cryoprotected in ascending sucrose solutions (10–30% sucrose w/v in 0.1 M PBS, pH 7.4, with 0.05% sodium

azide; Sigma-Aldrich; Rosene et al., 1986), frozen in isopentane (Fisher Scientific), at −80°C, and cut on a freezing microtome (AO Scientific Instruments, Reichert Technologies), in 50 $\mu$m coronal sections forming 10 series. Sections were stored free floating at −20°C in a solution of 30% ethylene glycol, 30% glycerol, and 0.05% sodium azide in 0.05 M phosphate buffer, pH 7.4.

### Bright-field and confocal microscopy

*Immunohistochemistry.* Free-floating sections were incubated for 1 h at 4°C in 0.05 M glycine (Sigma-Aldrich) and preblocked for 1 h at 4°C in 5% normal goat serum (NGS; Vector Laboratories), 5% bovine serum albumin (BSA; Sigma-Aldrich), and 0.2% Triton-X (Sigma-Aldrich) in 0.01 M PBS. For cases using BDA tracer, sections were incubated for 1 h at 25°C with avidin-biotin horseradish peroxidase (AB-HRP; Vectastain Elite ABC kit, Vector) at a 1:100 dilution in PBS, followed by rinses in PBS (all rinses are 3 × 10 min unless otherwise indicated), and tracer was visualized with incubation for 1–3 min in diaminobenzidine (DAB substrate kit, Vector). For cases with fluorescent tracer injections, sections were first incubated with avidin-biotin blocking solutions (AB blocking kit, Vector), and then rinsed in PBS and incubated overnight at 4°C with primary antibodies to tracers [FE (Invitrogen, catalog #A889; RRID: AB_221561), FR (Invitrogen, catalog #A6397; RRID: AB_1502299), CBL (Invitrogen, catalog #A5760; RRID: AB_11181009), or LY (Invitrogen, catalog #A5750 RRID:AB_1501344) at 1:800 in 1% NGS, 1% BSA, and 0.1% Triton-X in PBS; all rabbit polyclonal IgG]. Sections were then rinsed in PBS and incubated for 2 h at 25°C with biotinylated secondary antibodies (1:200 in 1% NGS, 1% BSA, and 0.1% Triton-X in PBS; biotinylated goat anti-rabbit IgG; Vector, catalog #BA-1000; RRID: AB_2313606), followed by AB-HRP and DAB, as above.

Sections were rinsed in 0.1 M phosphate buffer (PB), pH 7.4, mounted on gelatin-coated glass slides, and dried for ≥10 d. Slides were defatted in a 1:1 chloroform–ethanol mixture for 1 h and then rehydrated in a series of ethanols (100, 95, 70%) and then water, followed by staining with 0.05% thionin and rinsed again in water. Slides were then dehydrated in a series of ethanols (70, 95, 100%), cleared in xylene (Sigma-Aldrich), and coverslipped with Entallan mounting medium (Sigma-Aldrich).

For analysis with confocal microscopy, tissue was incubated in glycine and preblocked as above. Tracers and calcium-binding proteins were bound overnight at 4°C with primary antibodies [FE, FR, CBL, or LY: 1:800 in 1% NGS, 1% BSA, and 0.1% Triton-X in PBS; and CB (Swant, catalog #300, RRID: AB_10000347), CR (Swant, catalog #6B3, RRID: AB_1000032), or PV (Swant, catalog #235, RRID: AB_10000343) at 1:2000, mouse monoclonal, Swiss Antibodies]. Next, the tissue was rinsed in PBS and incubated overnight at 4°C in secondary antibodies conjugated with fluorescent label [1:100 in 1% NGS, 1% BSA, and 0.1% Triton-X in PBS; Alexa 568 goat anti-rabbit IgG (Invitrogen, catalog #11011, RRID: AB_143157) or goat anti-mouse IgG (Invitrogen, catalog #A11019, RRID: AB_143162) and Alexa 488 goat anti-mouse IgG (Invitrogen, catalog #A11001, RRID: AB_10566289) or goat anti-rabbit IgG (Invitrogen, catalog #A11008, RRID: AB_143165)]. Sections were rinsed in PB, mounted on gelatin-coated glass slides, and coverslipped while damp with Prolong Gold Antifade mounting medium (Invitrogen).

In all cases, primary and secondary antibody penetration was enhanced with 8 min runs (3 min on, 2 min off, 3 min on) in a temperature-

controlled variable-wattage microwave oven (150 W at 4°C, Pelco Biowave with ColdSpot and ThermoCube, Ted Pella) during each incubation. For three cases (BB, BN, and BO), a method of antigen retrieval was used before immunohistochemistry to enhance signal: sections were rinsed in PB, then incubated in 0.01 M sodium citrate buffer, pH 8.5, at 35–45°C for 30 min, followed by incubation in glycine, preblocking, and immunohistochemistry as above (Jiao et al., 1999). In control experiments omission of the primary antibodies and incubating in secondary antibody solutions showed no immunolabeling.

*Data analysis.* We used thionin-stained tissue to determine cytoarchitectonic and laminar boundaries of area OPro and area 32 (A32) in prefrontal cortex (Barbas and Pandya, 1989). OPro is dysgranular, contains a layer 2, and has slightly more prominent deep layers compared with upper layers (Barbas and Pandya, 1989). A32 is also dysgranular, has a broad layer 1, and a greater density of neurons in deep layers compared with upper layers (Dombrowski et al., 2001). All analyses were conducted in area OPro and A32 in the anterior cingulate. We refer to these areas as pOFC (OPro) and ACC (A32) for short, and based on their common references in the primate literature by location.

Columns with DAB-labeled amygdalar or thalamic fibers within pOFC or A32 were photographed at 1000× covering equal volumes of cortex in layer 1, layers 2–3a, layers 3b–5a, and layers 5b–6 (Olympus BX51 and DP70, Olympus). The maximum diameter of each labeled bouton was measured using the program Reconstruct (Synapse Web Reconstruct, RRID: nif-0000-23420; Fiala, 2005). At least four columns were analyzed to sample evenly across cortical areas; additional columns were sampled until ≥1000 boutons were identified in each case, which is sufficient to obtain a significant result using a Cohen's *d* power analysis for an effect size of 0.2 (Cohen, 1988). Statistical analyses were performed using Statistica software (version 10, StatSoft). Boutons were classified as large or small using a *k*-means cluster analysis for two clusters in each case and each area (cutoff between small and large ranged from 0.91 to 1.26 μm). We used two-tailed *t* tests to compare mean diameters across areas and pathways, and ANOVA with Bonferroni's *post hoc* analysis to compare bouton size distributions across areas and pathways.

We determined the density of small and large labeled amygdalar boutons in layers 1, 2–3a, and 3b–5a of pOFC and A32. For comparison, we also include areas 9/46, which are granular areas with well delineated six layers. We determined densities using a semiautomated method of systematic random sampling using a microscope fitted with a motorized stage and controlled by software (StereoInvestigator 10, MBF Biosciences; Olympus BX60). After pilot studies to determine the optimal sampling rate for each case and layer, we used a counting frame of 50 × 50 μm, disector height of 11 μm, and a counting frame size that varied from 100 × 100 μm to 750 × 750 μm to achieve a Gundersen coefficient of error (*m* = 1) <0.1. A cutoff of 1 μm was used to distinguish between small and large boutons for all cases and all layers, which is approximately the average of all cutoff values calculated (mean cutoff value, 1.1 μm; *n* = 12 cases). Densities were normalized to the densest area in each case, and we compared normalized densities across areas using ANOVA with Bonferroni's *post hoc* analysis.

We used laser scanning confocal microscopy (Fluoview FV-300, Olympus; LSM-510, Carl Zeiss Microscopy) to study appositions between fluorescently labeled tracer and dendrites labeled for calcium-binding proteins CR, CB, and PV. Stacks of optical sections 0.3 μm thick were acquired in columns of pOFC containing labeled fibers in layers 1–3a and 3b–5a, and all labeled boutons and appositions between labeled amygdalar or thalamic boutons and labeled dendrites were counted. Appositions were defined as close contacts between a labeled bouton and labeled dendrite, including an area of colocalization at the point of contact. Alexa 488 conjugates were excited with a 488 nm Argon laser. Alexa 568 conjugates were excited with a 568 nm krypton laser (Olympus) or 543 nm helium neon laser (Zeiss). We used $\chi^2$ tests to compare proportions of labeled axons forming appositions with labeled dendrites across pathways and layers.

## Electron microscopy
*Immunohistochemistry and embedding.* To study pathways in the electron microscope, we used triple immunohistochemistry to identify tracers with DAB (which appears as uniform dark precipitate under electron microscopy), and calcium-binding proteins (CB, PV, or CR) using gold labeling with silver enhancement (forms clumps of round particles) and tetramethylbenzidine (TMB) staining (forms rod-shaped precipitate), modified from previous studies (Medalla et al., 2007). Tissue sections were incubated as above in 0.01 M sodium citrate, pH 8.5 (30 min at 35°C), 0.05 M glycine (1 h at 4°C), and any BDA tracer was blocked with AB blocking solutions. Background binding was blocked with incubation for 1 h at 4°C in 5% NGS, 5% BSA, 0.025% Triton X-100 (Roche Applied Science), 0.1% acetylated BSA-c (Aurion), and 3.5% mouse blocking reagent (MOM basic kit, Vector) in PBS. Sections were then bound overnight at 4°C with antibodies for tracers [FE, FR, or LY: 1:800 in 1% NGS, 1% BSA, 0.1% BSA-c, 0.025% Triton X-100, and 8% MOM protein concentrate (MOM basic kit, Vector) in PBS; rabbit polyclonal IgG, Invitrogen] and one of three calcium-binding proteins (CB, CR, or PV: 1:2000, mouse monoclonal IgG, Swant). All primary and secondary antibody incubations included an 8 min microwave run as above.

Sections were rinsed in PBS then incubated for 6 h at 25°C with biotinylated secondary antibodies for tracers [1:200 in 1% NGS, 1% BSA, 0.1% BSA-c, 0.025% Triton X-100, 8% MOM protein concentrate, and 0.1% cold water fish gelatin (Aurion) in PBS; biotinylated goat anti-rabbit IgG (Vector)] and gold-conjugated secondary antibodies for calcium-binding proteins [1:50 UltraSmall ImmunoGold F(ab) fragment of goat anti-mouse IgG [Aurion, catalog #800.266, RRID: AB_2315632)]. Sections were then postfixed with 3% glutaraldehyde and 1% paraformaldehyde in PB in a microwave oven (2 min at 150 W, 4°C). Sections were rinsed in glycine (5 min) and rinsed in PB (2 × 10 min), followed by enhancement conditioning solution (ECS, 1:10, 2 × 10 min; Aurion). Gold-conjugated proteins were visualized by silver enhancement for 60–90 min (R-Gent SE-EM, Aurion); the tissue was then rinsed in ECS (2 × 10 min) and then PB (2 × 10 min). Tracers were visualized with DAB as above. For all rinses following silver enhancement, 0.1 M PB, pH 7.4, was used, and in some pieces of tissue the order of labeling was reversed to control for any attraction between gold and biotin. Any remaining biotin-binding sites were blocked with AB blocking solutions, and then any remaining mouse binding sites were blocked with incubation for 1 h at 4°C in 3.5% mouse blocking reagent, 5% NGS, 5% BSA, 0.025% Triton X-100, and 0.1% BSA-c in PB.

Sections were incubated overnight at 4°C with antibody for a second calcium-binding protein (CB, PV, or CR: 1:2000 in 1% NGS, 1% BSA, 0.1% BSA-c, 0.025% Triton X-100, and 8% MOM protein concentrate in PB; mouse monoclonal IgG, Swant), followed by rinses in PB and incubation for 1–2 h at 25°C in biotinylated secondary antibody (1:200 in 1% NGS, 1% BSA, 0.1% BSA-c, 0.025% Triton X-100, and 8% MOM protein concentrate in PB; biotinylated goat anti-mouse IgG, Vector), then rinsed in PB and incubated in AB-HRP as above. These calcium-binding proteins were visualized with TMB staining as follows: sections were first incubated for 15 min in 0.005% TMB (Sigma-Aldrich), 0.004% ammonium chloride (Sigma-Aldrich), and 5% ammonium paratungstate (Sigma-Aldrich) in 0.1 M PB, pH 6.0, and then incubated for 1–5 min in the same solution plus 0.005% hydrogen peroxide (Sigma-Aldrich) until staining appeared. The staining was stabilized by incubating sections for 10 min in a solution of 0.05% DAB (SigmaFast DAB tablet, Sigma-Aldrich), 0.02% cobalt chloride (Sigma-Aldrich), 0.004% ammonium chloride (Sigma-Aldrich), and 0.005% hydrogen peroxide (Sigma-Aldrich) in 0.1 M PB, pH 6.0. Finally, sections were rinsed in PB and postfixed in 6% glutaraldehyde and 2% paraformaldehyde in PB with a microwave oven (150 W at 15°C) until sample temperature reached 30–35°C (Jensen and Harris, 1989). We conducted control experiments on tissue by omitting primary antibodies and incubating in secondary antibody solutions and no immunolabeling was observed.

Sections were rinsed in PB (3 × 20 min) and postfixed for 15 min in 1% osmium tetroxide (Electron Microscopy Sciences) with 1.5% potassium ferrocyanide (Electron Microscopy Sciences) in PB with a microwave oven (100 W at 12°C; 2 min on, 2 min off, 2 min on) and rinsed in PB (3 × 2 min) and water (3 × 2 min). Sections were then rinsed in 50% ethanol (3 × 5 min), stained with 1% uranyl acetate (30 min in 70% ethanol; Electron Microscopy Sciences), and dehydrated in a series of ethanols (90, 95, 100%; 3 × 5 min each). For embedding, sections were
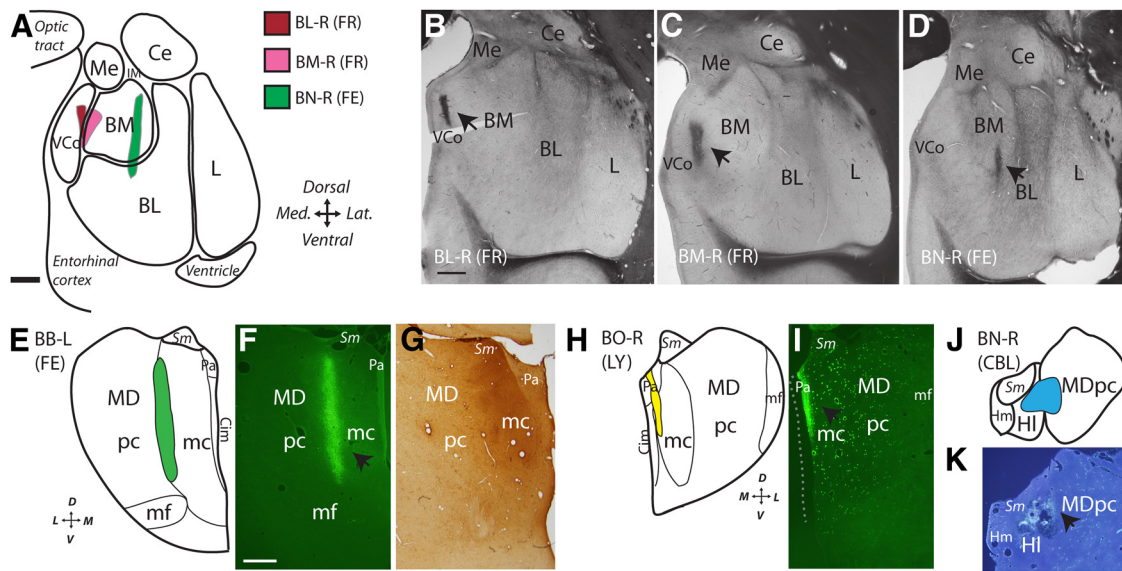
**Figure 1.** *A–K*, Injection sites in the amygdala (*A–D*) and mediodorsal thalamus (*E–K*). Scale bars, 1 mm. *A*, Schematic shows relative position of small injection sites in the amygdala in cases BL-R, BM-R, and BN-R. *B–D*, Fresh tissue sections show tracer in the amygdala (arrows). *E, H, J*, Schematics depict location of tracer injections in thalamic mediodorsal nucleus (cases BB-L, BO-R, and BN-R). *F, I, K*, Fluorescent micrographs show tracer in the thalamus. *G*, Bright-field photomicrograph shows section with injection in MD magnocellular. BL, Basolateral nucleus; BM, basomedial nucleus; CBL, cascade blue; Ce, central nucleus; Cim, central intermediate nucleus; FE, fluoroemerald; FR, fluororuby; L, lateral nucleus; LY, Lucifer yellow; mc, magnocellular sector; mf, multiform sector; pc, parvicellular sector; Sm, stria medularis; VCo, ventral cortical nucleus.

infiltrated with propylene oxide (2 × 7 min; Electron Microscopy Sciences), and then a 1:1 mixture of Araldite (Electron Microscopy Sciences) and propylene oxide (1 h). Sections were infiltrated with Araldite overnight, followed by flat embedding in Araldite in aclar (Ted Pella). Aclar-embedded tissue was cured for 48 h at 60°C. Small columns of tissue 500–750 μm wide were cut from each section, divided by layer, re-embedded in Araldite blocks, and cured for 48 h at 60°C.

*Serial sectioning and data analysis.* To reconstruct postsynaptic sites, Araldite blocks containing embedded tissue from layers 1, 2–3a, or 3b–5a were sectioned at 50 nm using an ultramicrotome (Leica Ultracut UCT, Leica Microsystems) and collected on pioloform-coated copper slot grids, to form series of ~75–150 sections. Using 80 kV transmission electron microscope at 16,000–26,000× (JEOL 100CX, Jeol), we exhaustively sampled a few sections to identify ~10–30 labeled boutons in each series. Each bouton was photographed in serial sections through the entire bouton plus five additional sections before and after. We analyzed labeled boutons using Reconstruct to trace bouton profiles and postsynaptic sites (Fiala, 2005). Synapses, axon terminals, and postsynaptic sites were identified using classical criteria (Peters et al., 1991), and all labeled boutons and postsynaptic sites that were complete in the series were reconstructed in 3D to determine volumes and area of the postsynaptic density (PSD). Models in 3D were generated in Reconstruct and imported into 3Ds Max for rendering (version 14, Autodesk). We determined extraneous background level of gold labeling in each piece of tissue (Muly et al., 2009; Medalla and Barbas, 2012). In one series for each piece of tissue, enhanced gold particles in mitochondria were counted, and this value was divided by the total volume of mitochondria in the series. The threshold for gold-positive elements was set to twice the density of gold in mitochondria. We compared mean diameters, bouton and spine volumes, and PSD areas across pathways using hierarchically nested mixed-model ANOVA for comparisons including boutons from multiple cases, and proportions of synaptic specializations using Fisher exact tests. We used linear regression to analyze correlation between bouton volume and PSD area or spine volume.

We also used systematic random sampling to analyze unlabeled boutons in the neuropil surrounding labeled amygdalar boutons. In one of every 20 series in case BN-R, we measured the PSD area for all unlabeled asymmetric synapses that were complete in the series, using Reconstruct. We compared the PSD area of unlabeled synapses and labeled amygdalar synapses using a two-tailed *t* test.

## Results

### Injection sites in the amygdala and MD

The pathways studied with neural tracers are shown in Figure 1 and listed in Table 1. We used cases with large injections in the amygdala (Ghashghaei et al., 2007) to study the overall pattern of amygdalar pathways, and smaller injections (Fig. 1A–D) to study specific aspects of amygdalar pathways at the level of the system and the synapse. The tracer injections in amygdalar nuclei are listed in Table 1; they include the basal and cortical nuclei that project extensively to pOFC in rhesus monkeys (Porrino et al., 1981; Barbas and De Olmos, 1990).

For comparison, we studied the pattern of thalamocortical pathways to pOFC and their synaptic interactions with light, confocal, and electron microscopy. Targeted small injections of tracer in two cases were mainly localized in MD magnocellular, including its junction in one case with MD parvicellular (MDpc; Fig. 1E–G), and in another case with part of the paraventricular (Pa) nucleus (Fig. 1H,I). A third small injection included caudal MDpc (Fig. 1J,K). All of these segments of MD and Pa are connected strongly with pOFC (Dermon and Barbas, 1994). In the third case, the tracer spread to part of the habenula (Fig. 1J,K), which projects mainly to the brainstem (Shelton et al., 2012); we used this case to study thalamocortical pathways with light microscopy.

### Amygdalar terminals were densest in pOFC

First we studied the density of amygdalar terminations in pOFC compared with the density in prefrontal A32 and areas 9/46 (Fig. 2A–I). Like pOFC, A32 in the ACC has a dysgranular structure and is phylogenetically old, but the two areas have different functions (for review, see Barbas, 1997). On the other hand, dorsolateral prefrontal areas 9/46 differ markedly from either pOFC or ACC by having a six-layer (eulaminate) structure (Barbas and Pandya, 1989) and a role in cognitive operations (Miller and Cohen, 2001; Wallis et al., 2001).
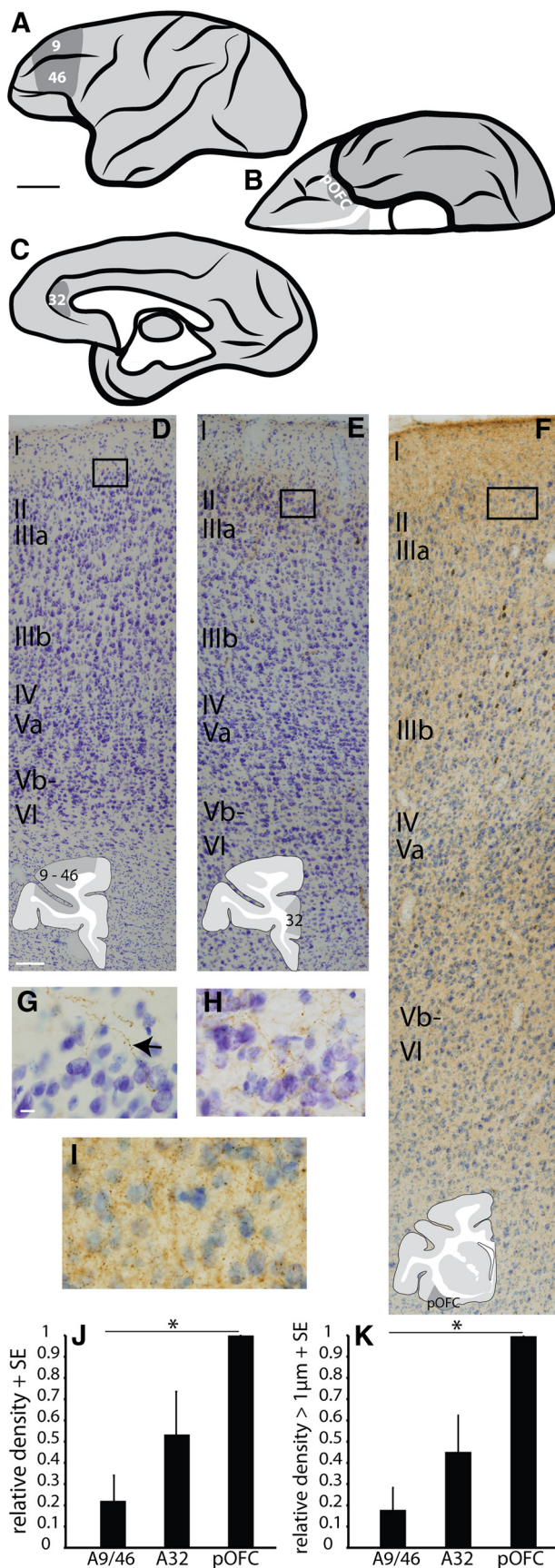
We found that amygdalar terminals were consistently most dense in pOFC ($n = 3$ cases for each of three areas; ANOVA with Bonferroni's *post hoc* test, $F_{(2,6)} = 5.5$, $p = 0.05$ between pOFC and areas 9/46; Fig. 2J), confirming and extending previous findings (Ghashghaei et al., 2007). Each case showed the same density distribution pattern, with pOFC having the highest density of amygdalar terminals, areas 9/46 the lowest, and A32 intermediate density. In each area, a higher proportion of boutons was found in the upper layers compared with the middle layers, and there were no significant differences among areas in this pattern.

### Amygdalar terminals were larger in pOFC than in other prefrontal areas

After measuring the major diameter of amygdalar boutons in pOFC and A32 in a large population ($n = 31,420$ boutons in pOFC; $n = 16,967$ boutons in A32), we performed a *k*-means cluster analysis, which separated boutons into two groups by diameter: large and small. We used a cutoff of 1 $\mu$m to distinguish between small and large boutons for all cases and all layers, which is approximately the average of all cutoff values calculated (mean cutoff value, 1.1 $\mu$m; $n = 12$ cases). The rationale is based on evidence that bouton size is highly correlated with the number of synaptic vesicles, and with the synaptic efficacy of the pathway (Germuska et al., 2006). We then compared the density of large amygdalar boutons ($\geq 1$ $\mu$m in diameter) in the three prefrontal sites. We found that pOFC also contained the highest density of large amygdalar boutons ($n = 3$ cases in each of three areas; ANOVA with Bonferroni's *post hoc* test, $F_{(2,6)} = 8.5$, $p = 0.02$ between pOFC and areas 9/46; Fig. 2K).

Next we compared directly the size of amygdalar terminals in pOFC and in A32. We found that amygdalar terminals across all layers in pOFC were larger than those in A32, though not significantly (mean diameter $\pm$ SE: pOFC, $1.0 \pm 0.021$ $\mu$m, $n = 6$ cases; A32, $0.97 \pm 0.0057$ $\mu$m, $n = 3$; two-tailed *t* test, $t_{(7)} = 1.9$, $p = 0.1$). By comparing the frequency of large boutons, we found that the amygdalar projection to pOFC contained significantly more large boutons than A32 (1–1.5 $\mu$m diameter; pOFC, $n = 6$ cases and 8 bins; A32, $n = 3$ cases and 8 bins; multifactorial ANOVA with Bonferroni's *post hoc* test, $F_{(7,56)} = 30.6$, $p = 0.002$; Fig. 3A). These data show that pOFC receives denser projections as well as a higher proportion of large terminals from the amygdala compared with A32, another phylogenetically old prefrontal area that is also strongly connected with the amygdala.

### Amygdalar terminals were larger than thalamic terminals in pOFC

We then compared amygdalar terminals in pOFC with terminals from the thalamic MD nucleus, which is the major source of thalamic input to pOFC (Goldman-Rakic and Porrino, 1985; Dermon and Barbas, 1994). Across all layers of pOFC, amygdalar terminals were larger than those from MD (mean diameter $\pm$ SE: amygdalar, $1.0 \pm 0.021$ $\mu$m, $n = 6$ cases with 31,420 boutons; thalamic, $0.88 \pm 0.050$ $\mu$m, $n = 3$ cases with 7,169 boutons; two-tailed *t* test, $t_{(7)} = 2.8$, $p = 0.03$). We further characterized the frequency of large boutons and found that compared with

←

9/46 (**D,** A9/46); A32 (**E**); and pOFC (**F**, area OPro) labeled for amygdalar fibers (**G–I**, insets). Scale bar: (in **D**) **D–F**, 100 $\mu$m. **G–I**, Amygdalar fibers (arrow) at layer 1–2 border in A9/46 (**G**), A32 (**H**), and pOFC (**I**). Scale bar: (in **G**) **G–I**, 10 $\mu$m. **J**, Relative density of amygdalar boutons in A9/46, A32, and pOFC, normalized to the highest density in each case (pOFC). **K**, Relative density of large amygdalar boutons $\geq 1$ $\mu$m in diameter in A9/46, A32, and pOFC, normalized to the highest density in each case (pOFC). Vertical lines indicate SE. *$p \leq 0.05$.

**Figure 2.** Amygdalar boutons were densest and largest in pOFC. **A–C**, Areas of study: lateral (**A**), orbital (**B**), and medial (**C**) views of a rhesus monkey brain show areas of interest in areas 9/46, OPro (pOFC), and A32 (ACC). Scale bar, 1 cm. **D–F**, Nissl-stained columns of cortex in areas
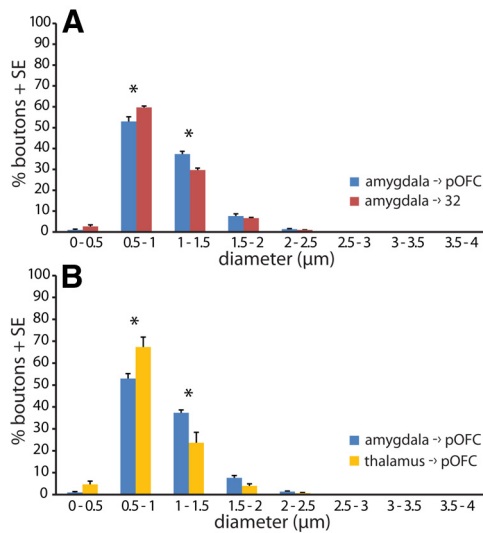
**Figure 3.** Amygdalar axon boutons in pOFC were larger than in A32 or the thalamic. *A*, Histogram shows size distribution of amygdalar boutons in A32 (red) and pOFC (blue) across all layers. *B*, Histogram shows size distribution of amygdalar boutons (blue) and thalamic boutons (yellow) in pOFC across all layers. Vertical lines indicate SE. *$*p \leq 0.05$.

boutons from MD, the amygdalar projection to pOFC contained a significantly higher proportion of large boutons (1–1.5 $\mu$m diameter: amygdalar, $n = 6$ cases and 8 bins; thalamic, $n = 3$ cases and 8 bins; multifactorial ANOVA with Bonferroni's *post hoc* test, $F_{(7,56)} = 9.5, p = 0.0001$; Fig. 3B).

Next we analyzed the middle cortical layers specifically (layers 3b–5a), which are thought to be the primary recipient of driver thalamocortical fibers. We found that amygdalar terminals (mean diameter $\pm$ SE, 1.06 $\pm$ 0.026 $\mu$m, $n = 6$ cases) were significantly larger than the thalamic even in the middle layers (layers 3b–5a: 0.89 $\pm$ 0.047 $\mu$m, $n = 3$; two-tailed *t* test, $t_{(7)} = 3.1$, $p = 0.02$), which is consistent with the pattern shown above.

Analysis of boutons measured at the synaptic level in the electron microscope confirmed the data obtained at the light microscope (mean diameter $\pm$ SE, 0.99 $\pm$ 0.033 $\mu$m, $n = 164$ amygdalar boutons from two cases; 0.84 $\pm$ 0.041 $\mu$m, $n = 39$ thalamic boutons from two cases; hierarchically nested mixed-model ANOVA, $F_{(1,5.7)} = 10.7$ for fixed effect of injection site, $p = 0.02$; $F_{(2,199)} = 0.3$ for random effect of case, $p = 0.7$; Fig. 4A–H). When reconstructed in 3D, amygdalar boutons were larger in volume (mean volume $\pm$ SE, 0.33 $\pm$ 0.035 $\mu$m$^3$, $n = 152$ boutons from two cases) than the thalamic (0.19 $\pm$ 0.024 $\mu$m$^3$, $n = 36$ boutons from two cases; hierarchically nested mixed-model ANOVA, $F_{(1,20.6)} = 14.6$ for fixed effect of injection site, $p = 0.001$; $F_{(2,183)} = 0.1$ for random effect of case, $p = 0.9$; Fig. 4I). These results show that amygdalar boutons in the upper layers of pOFC are even larger than thalamic boutons forming synapses in the middle layers; the latter form a robust pathway in sensory systems that reliably relays information from the thalamus to cortex (Sherman and Guillery, 1998).

**Appositions between amygdalar and thalamic projections with inhibitory neurons**

A key unanswered question about the amygdalar and thalamic pathways is the nature of their postsynaptic targets in pOFC. With regard to cortical inhibitory neurons, the upper layers (1–3a) of pOFC are populated mostly by two classes of inhibitory neurons: CR-positive (Fig. 5A, green) presumed inhibitory neurons, which form synapses on neighboring inhibitory

neurons, at least in the upper layers of some areas, and CB-positive (Fig. 5A, red) inhibitory neurons, which form synapses on the dendrites of nearby pyramidal neurons in layers 2–5 (DeFelipe, 1997). The middle–deep layers (3b–6) contain mostly PV-positive (Fig. 5A, blue) inhibitory neurons, which provide strong inhibition by forming synapses on the soma, axon initial segment, or proximal dendrites of layer 3 and 5 pyramidal neurons (DeFelipe, 1997).

We first studied the prevalence of appositions between amygdalar fibers and PV, CB, and CR inhibitory neurons in pOFC using laser scanning confocal microscopy ($n = 376$ appositions of 8,035 boutons in two cases; Fig. 5B,C). Of the three classes of presumed inhibitory neurons, amygdalar projections in the upper layers of pOFC formed appositions mostly with CB (8%; Fig. 5F) and CR neurons (8%) and less often with PV neurons (2%). By comparison, in the middle layers of pOFC, amygdalar boutons formed fewer appositions with CB (2%, $\chi^2_{(1, n = 2232)} = 41.9, p < 0.00001$; Fig. 5F) or CR neurons (3%, $\chi^2_{(1, n = 2771)} = 13.9\ p = 0.0002$) and more with PV neurons (4%, $\chi^2_{(1, n = 3203)} = 13.4, p = 0.0003$).

We then studied appositions between thalamic terminals and inhibitory neurons in the middle layers (3b–5a) of pOFC, which are the predominant layers innervated by thalamic afferents ($n = 101$ appositions of 1,226 boutons in two cases; Fig. 5D,E). Thalamic terminals, compared with amygdalar terminals, targeted a greater proportion of inhibitory neurons in the middle layers. Specifically, thalamic axons formed more appositions with PV (11%, $\chi^2_{(1, n = 1498)} = 24.5, p < 0.00001$; Fig. 5G) or CR neurons (10%, $\chi^2_{(1, n = 941)} = 15.4, p = 0.0001$), and a similar proportion with CB neurons (3%).

In a case with a more medial injection of tracer (Fig. 1H,I; case BO-R), thalamic afferents terminated in significant numbers in the upper layers of pOFC as well ($n = 123$ appositions of 1,156 boutons). Compared with amygdalar axons in the upper layers of pOFC, thalamic axons targeted significantly more CB neurons (14%, $\chi^2_{(1, n = 1834)} = 13.2, p = 0.0003$) and a similar proportion of CR neurons (7%). Meanwhile, no boutons formed appositions with PV neurons. Consistent with these findings, midline and paralaminar thalamic nuclei activate feedforward inhibition in upper cortical layers in mice (Cruikshank et al., 2012). These data show that, compared with amygdalar fibers, thalamic fibers targeted a higher proportion of inhibitory neurons in both the upper and middle layers of pOFC.

A few amygdalar axons targeted inhibitory neurons proximally in the upper layers of pOFC, forming significantly more appositions on cell bodies of inhibitory neurons in layers 1–3a ($n = 11$ of 310 appositions: 7 CB positive, 3 PV positive, 1 CR positive) than thalamic axons, which formed no appositions involving a soma ($n = 0$ of 123 appositions; $\chi^2_{(1, n = 433)} = 4.5, p = 0.03$). On the other hand, in the middle layers of pOFC, both amygdalar and thalamic axons formed appositions with cell bodies of presumed inhibitory neurons ($n = 5$ of 224 thalamic appositions; $n = 1$ of 66 amygdalar appositions; all PV positive; Fig. 5D). This suggests that, although amygdalar fibers interacted with relatively fewer inhibitory neurons in the upper layers of pOFC, they targeted inhibitory neurons more proximally than the thalamic pathways.

**Postsynaptic targets of amygdalar projections in pOFC**

We further investigated at the synaptic level the excitatory and inhibitory targets of amygdalar terminals in pOFC. We reconstructed synapses formed between amygdalar axons and elements of postsynaptic neurons in the upper layers (1–3a) of pOFC using
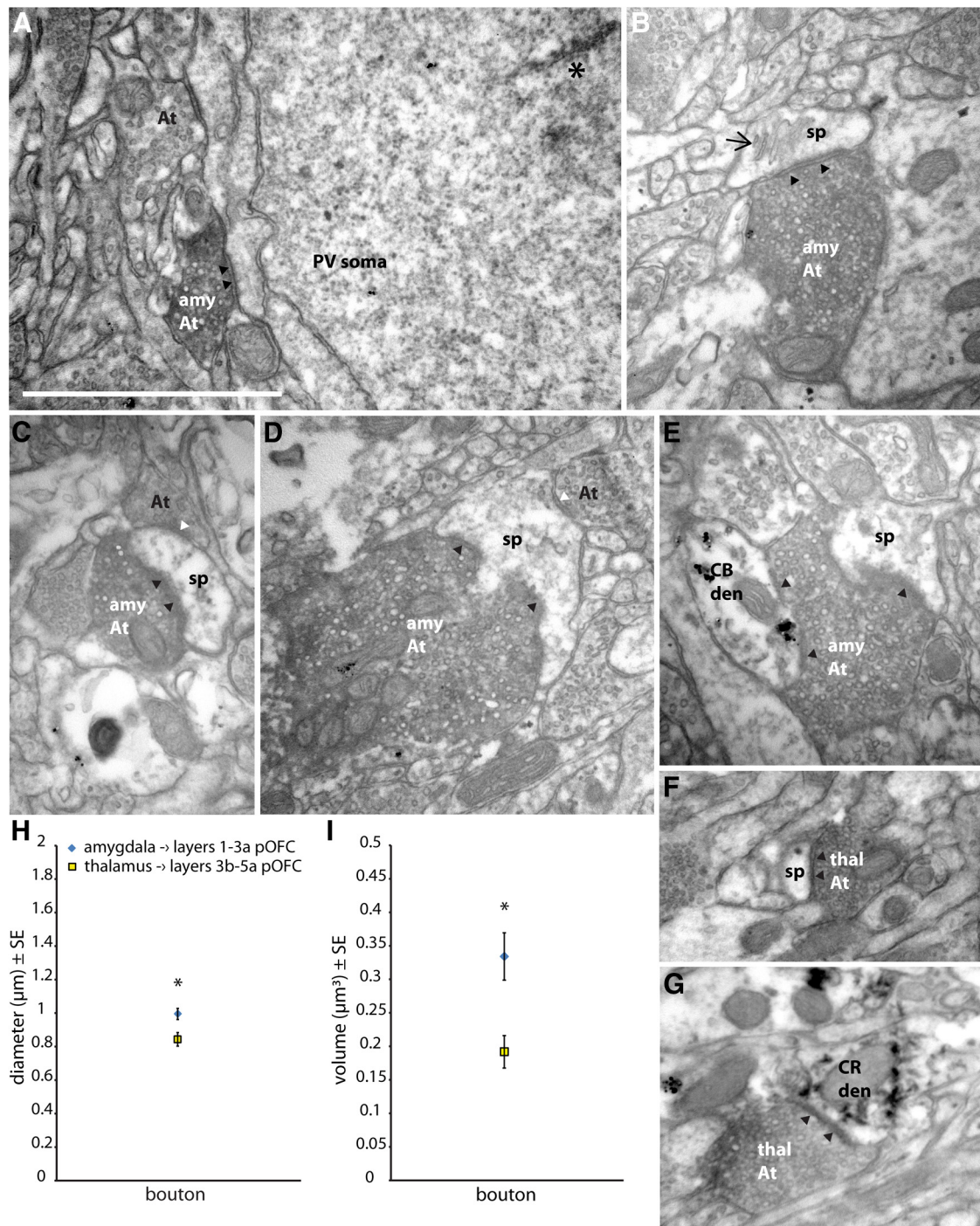
**Figure 4.** Amygdalar terminals in the upper layers of pOFC were larger than thalamic terminals in the middle layers at the synaptic level. Scale bar: (in **A**) **A–G**, 1 μm. **A–E**, Amygdalar boutons labeled with DAB in the upper layers of pOFC, forming (**A**) a macular synapse (silhouette arrowheads) with a PV-positive soma labeled with TMB (asterisk); (**B**) a macular synapse (black arrowheads) with a spine (sp) containing a spine apparatus (arrow); (**C**) A macular synapse (black arrowheads) with a spine (sp), which also receives an unlabeled symmetric synapse (white arrowhead) from a presumed inhibitory bouton (At); (**D**) a perforated synapse (black arrowheads) with a spine (sp), which also receives an unlabeled symmetric synapse (white arrowhead) from a presumed inhibitory bouton (At); (**E**) Two synapses (black arrowheads) with a spine (sp) and a CB-positive dendrite (CB den) labeled with gold (black clumps). **F, G**, Thalamic boutons labeled with DAB forming (**F**) a macular synapse (black arrowheads) with a spine (sp) and (**G**) a macular synapse (black arrowheads) with a CR-positive dendrite (CR den) labeled with TMB. **H**, Diameters of amygdalar boutons in the upper layers of pOFC (blue) and thalamic boutons in the middle layers of pOFC (yellow), measured in the electron microscope. **I**, Amygdalar axon boutons in the upper layers of pOFC were larger in volume than thalamic terminals in the middle layers of pOFC. Vertical lines indicate SE. *$p \leq 0.05$. amy At, Amygdalar axon terminal; At, axon terminal; den, dendrite; thal At, thalamic axon terminal.

electron micrographs from uninterrupted serial sections through the synapse photographed in the electron microscope ($n = 164$ boutons from two cases; Fig. 6A–C). We identified postsynaptic targets by morphology for excitatory neurons, which have spiny dendrites, and by morphology and label for CB, CR, or PV for

presumed inhibitory neurons, which have smooth or sparsely spiny dendrites (Peters et al., 1991; DeFelipe, 1997).

The majority of amygdalar boutons innervated single spines of presumed excitatory neurons in the upper layers of pOFC (75%, $n = 123$ of 164 boutons; Fig. 6D). A smaller proportion
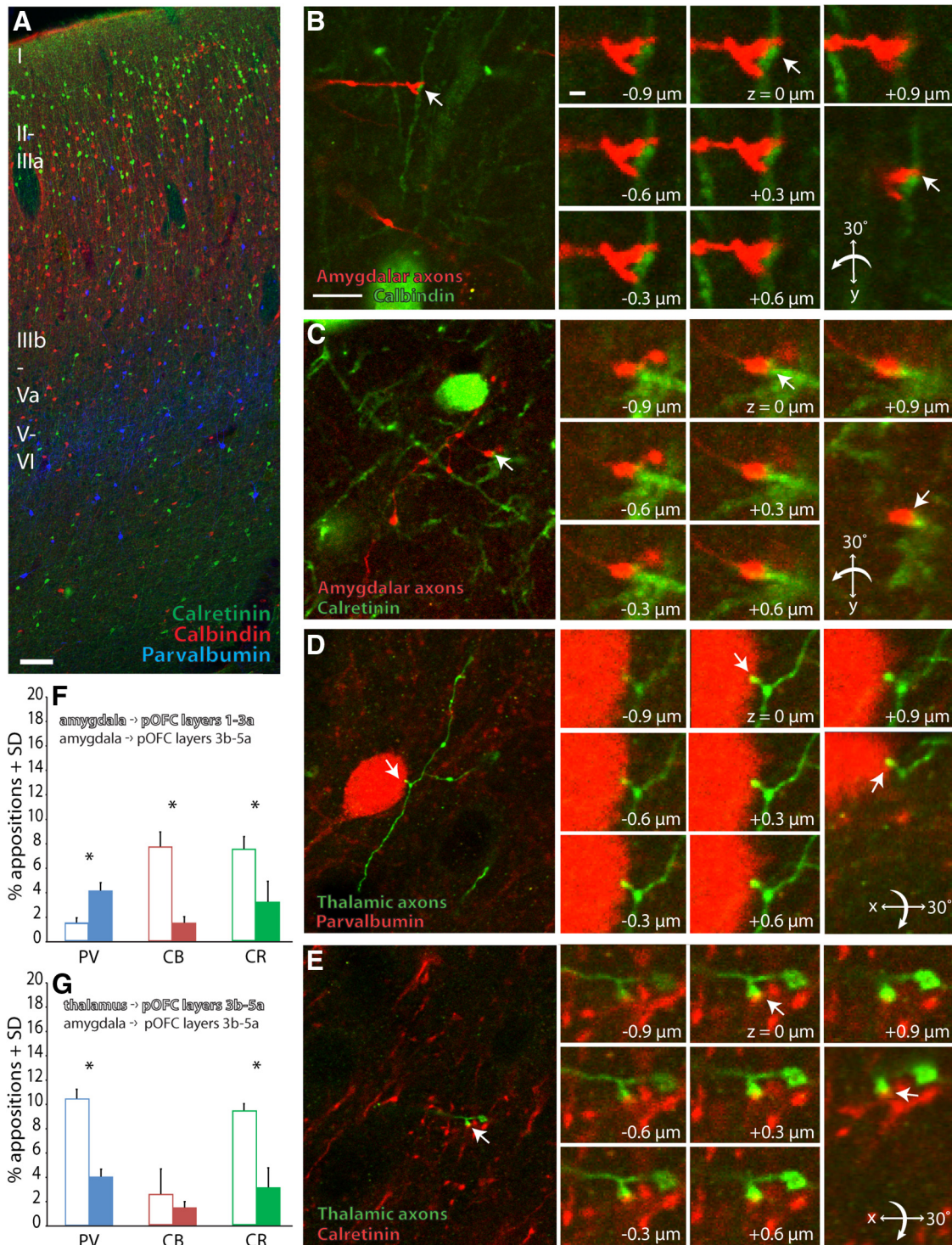
**Figure 5.** Examples of amygdalar and thalamic axons targeting inhibitory neurons in pOFC. **A**, Distribution of presumed inhibitory neurons shown in pseudocolor in pOFC, where CR neurons (green) and CB neurons (red) were found mostly in the uppers layers and PV neurons (blue) were found mostly in the middle–deep layers. Scale bar, 100 μm. **B**, Amygdalar axons (red) in the upper layers of pOFC; one is closely apposed to a dendrite of a CB neuron (green, white arrows). Scale bar: (in **B**, left) **B–E**, left, 10 μm. Right, Sequential optical sections through apposition and 3D rotation through apposition. Scale bar: (**B**, inset) **B–E**, insets, 1 μm. **C**, Amygdalar axons (red) in the upper layers of pOFC; one close apposition with a dendrite of a CR neuron (green, white arrows). **D**, Thalamic axon (green) in the middle layers of pOFC; example of a close apposition with a PV neuron (red, white arrows). **E**, Thalamic axon (green) in the middle layers of pOFC formed a close apposition with a CR neuron (red, white arrows). **F**, Amygdalar terminals targeted more CB and CR inhibitory neurons in the upper layers of pOFC (open bars), and more PV neurons in the middle layers (filled bars). **G**, Thalamic terminals (open bars) targeted more PV and CR neurons in the middle layers compared with amygdalar terminals (filled bars). Vertical lines indicate SD. *p ≤ 0.05.

(10%, n = 17) of amygdalar boutons formed synapses with single dendrites of presumed inhibitory neurons, and only one terminal formed a synapse with a soma. The remaining boutons were multisynaptic (14%, n = 23), which were more frequent in the amygdalar pathway than the thalamic (3%, n = 1 of 39 boutons; two-tailed Fisher exact test, p = 0.05; Fig. 6D). Of these multisynaptic amygdalar boutons, the majority formed a synapse with one dendrite and ≥1 spine (8%, n = 12 of 164 boutons) or
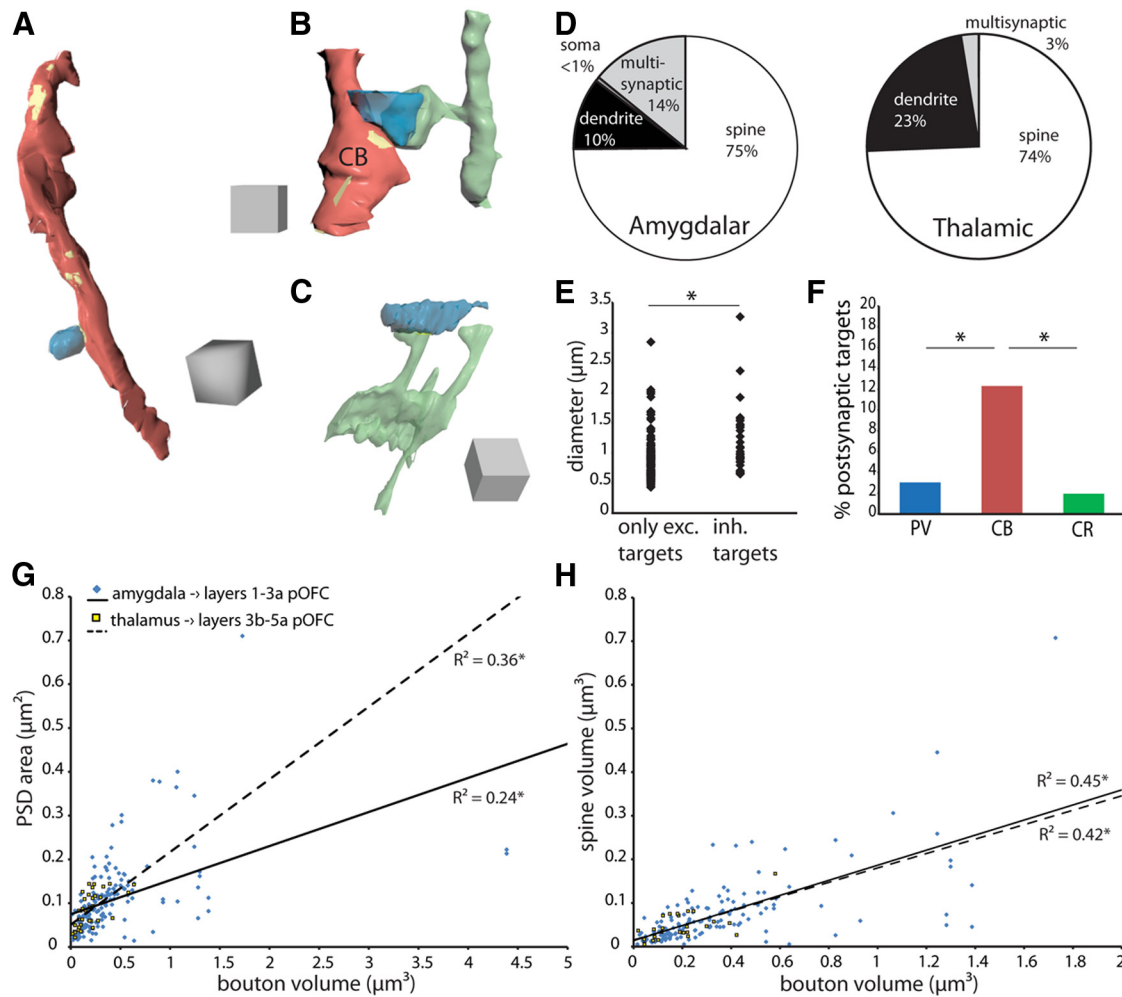
**Figure 6.** Excitatory and inhibitory postsynaptic targets of amygdalar boutons in pOFC. **A–C**, Amygdalar boutons (blue) form synapses (yellow) with (**A**) a smooth dendrite of a presumed inhibitory neuron (red), (**B**) a smooth dendrite (red) labeled for CB and a spiny dendrite of a presumed excitatory neuron (green), and (**C**) a spiny dendrite of a presumed excitatory neuron (green). Scale: cubes are 1 $\mu m^3$. **D**, Left, Amygdalar boutons most frequently innervated single spines in the upper layers of pOFC, and a significant proportion were multisynaptic. Right, Thalamic boutons also formed synapses mostly with spines, but thalamic pathways contained fewer multisynaptic boutons in the middle layers of pOFC. **E**, Amygdalar boutons with ≥1 inhibitory target were larger than amygdalar boutons with only excitatory targets. **F**, Among labeled dendrites, amygdalar boutons mostly formed synapses with CB-positive dendrites of presumed inhibitory neurons in the upper layers of pOFC. **G**, Amygdalar (blue diamonds, solid line) and thalamic (yellow squares, dashed line) bouton volume was positively correlated with PSD area. **H**, Amygdalar (blue diamonds, solid line) and thalamic (yellow squares, dashed line) bouton volume was positively correlated with spine volume. *$p ≤ 0.05$.

formed synapses with multiple spines (5%, $n = 9$), and a minority (<1%, $n = 1$) formed synapses with multiple dendrites or with a soma and multiple spines (<1%, $n = 1$).

Some amygdalar boutons in the upper layers of pOFC formed synapses with dendritic shafts of presumed inhibitory neurons (16% of synapses, $n = 31$ of 189 synapses total, formed by 164 labeled boutons). Boutons forming synapses with ≥1 dendritic shaft or soma (presumed inhibitory neurons) were significantly larger than boutons with only excitatory postsynaptic targets (mean diameter ± SE, 1.2 ± 0.094 $\mu m$, $n = 32$ boutons with inhibitory targets from two cases; 0.95 ± 0.033 $\mu m$, $n = 132$ boutons with excitatory targets from two cases; hierarchically nested mixed-model ANOVA, $F_{(1,2.1)} = 18.1$ for fixed effect of target, $p = 0.05$; $F_{(2,160)} = 0.4$ for random effect of case, $p = 0.6$; Fig. 6E). Among labeled dendrites, CB-positive dendrites were the most frequently innervated (12%, $n = 15$ dendrites of 122 boutons; Fig. 6F). Fewer amygdalar boutons formed synapses with PV (3%, $n = 2$ dendrites and 1 soma of 99 boutons; two-tailed Fisher exact test, $p = 0.01$) or CR neurons (2%, $n = 2$ dendrites of 105 boutons, $p = 0.004$). The remaining dendrites

and soma were unlabeled ($n = 13$ of 31 dendrites and 2 somata). These data are consistent with the fluorescence data (where 17% of boutons were apposed to a labeled dendrite or soma) but show a relatively greater proportion of synapses with CB neurons, and fewer with CR neurons (Figs. 5F, 6F). A minority of spines were labeled for CB (5%, $n = 6$ of 114 spines), which may belong to a minority of pyramidal neurons that are positive for CB, or only in one instance for PV (1%, $n = 1$ of 94 spines), which likely belongs to a sparsely spiny inhibitory neuron (DeFelipe, 1997). These data at the synaptic level highlight the role of CB neurons among inhibitory neurons targeted by the amygdala.

**Synaptic specializations of amygdalar and thalamic boutons**
The majority of synapses formed by amygdalar boutons were macular (Peters and Kaiserman-Abramof, 1969), with the post-synaptic density forming a complete disk (Fig. 4A–C). Some amygdalar synapses were perforated with a discontinuous PSD (21%, $n = 40$ of 189 synapses; Fig. 4D), most of which were on spines (80%, $n = 32$ of 40; the remainder were on dendrites). This was similar to the proportion of thalamic boutons forming per-

forated synapses in the middle layers (13%, $n = 5$ of 40 synapses, all axospinous). Among amygdalar and thalamic boutons, PSD area was significantly correlated with bouton volume (linear regression: amygdala, $n = 178$ boutons, $R^2 = 0.24$, $F_{(1,176)} = 54.1$, $p < 0.0001$; thalamus, $n = 36$ boutons, $R^2 = 0.36$, $F_{(1,34)} = 18.8$, $p = 0.0001$; Fig. 6G). The lower slope of the correlation between amygdalar bouton volume and PSD area may be due to the greater proportion of multisynaptic amygdalar boutons, compared with the thalamic pathway.

The volume of postsynaptic spines was also significantly correlated with bouton volume (linear regression: amygdala, $n = 145$ boutons, $R^2 = 0.45$, $F_{(1,143)} = 117.5$, $p < 0.0001$; thalamus, $n = 26$ boutons, $R^2 = 0.42$, $F_{(1,24)} = 17.3$, $p = 0.003$; Fig. 6H). Thalamic boutons in the middle layers targeted a significantly higher proportion of spines containing a spine apparatus (SA) or smooth endoplasmic reticulum (SER, 55%, $n = 16$ of 29 spines; two-tailed Fisher exact test, $p = 0.02$) compared with amygdalar boutons (32%, $n = 50$ of 156 spines; Fig. 4C). SER is found in dendrites and some spines, which at times forms an SA; these components are associated with stable spines (Ostroff et al., 2010). Additionally, a minority of amygdala-targeted spines in pOFC (5%, $n = 7$ of 156 spines; Fig. 4C,D) also received a symmetric synapse, presumably from a local inhibitory neuron. These results show that amygdalar boutons formed perforated synapses, larger synapses, and targeted larger spines.

**Comparison of amygdalar synapses with surrounding neuropil**
We next investigated whether the prevalence of large amygdalar synapses differs from nonlabeled synapses in the neuropil. This analysis revealed that amygdalar boutons formed synapses that were significantly larger than those in the surrounding neuropil (mean area ± SE, 0.11 ± 0.0064 $\mu m^2$, $n = 178$ amygdalar synapses from two cases; 0.84 ± 0.0052 $\mu m^2$, $n = 165$ unlabeled synapses from one case; two-tailed $t$ test, $t_{(341)} = 2.6$, $p = 0.01$).

## Discussion
Novel findings from the system to the synapse revealed that the pathway from the amygdala to pOFC is stronger than to other prefrontal cortices or even the thalamocortical pathway (Fig. 7). This conclusion is based on evidence that the amygdalar pathway to pOFC is denser (Ghashghaei et al., 2007), has more large terminals, is largely excitatory, and is distinguished for unique synaptic specializations among other pathways. In aggregate, these features suggest that the amygdala can exert a powerful influence on pOFC.

**Specialized amygdalar pathways target preferentially the pOFC: comparison with ACC**
We found that pathways from large or restricted amygdalar sites consistently innervated most robustly the pOFC than areas 9/46 or even ACC, which is also strongly linked with the amygdala (Ghashghaei et al., 2007). The amygdalar pathway to pOFC had a significant proportion of large terminals. Large terminals have a higher content of vesicles and mitochondria (Germuska et al., 2006; Zikopoulos and Barbas, 2007b), and are associated with greater synaptic efficacy and highly active synapses (Reichova and Sherman, 2004; Zikopoulos and Barbas, 2007b).

Among prefrontal areas, the pOFC is distinguished for receiving extensive projections from sensory association cortices representing each modality (for review, see Barbas, 2000). Coupled with robust input from the amygdala, the pOFC is poised to link external cues with internal valuations, reliably convey the salience
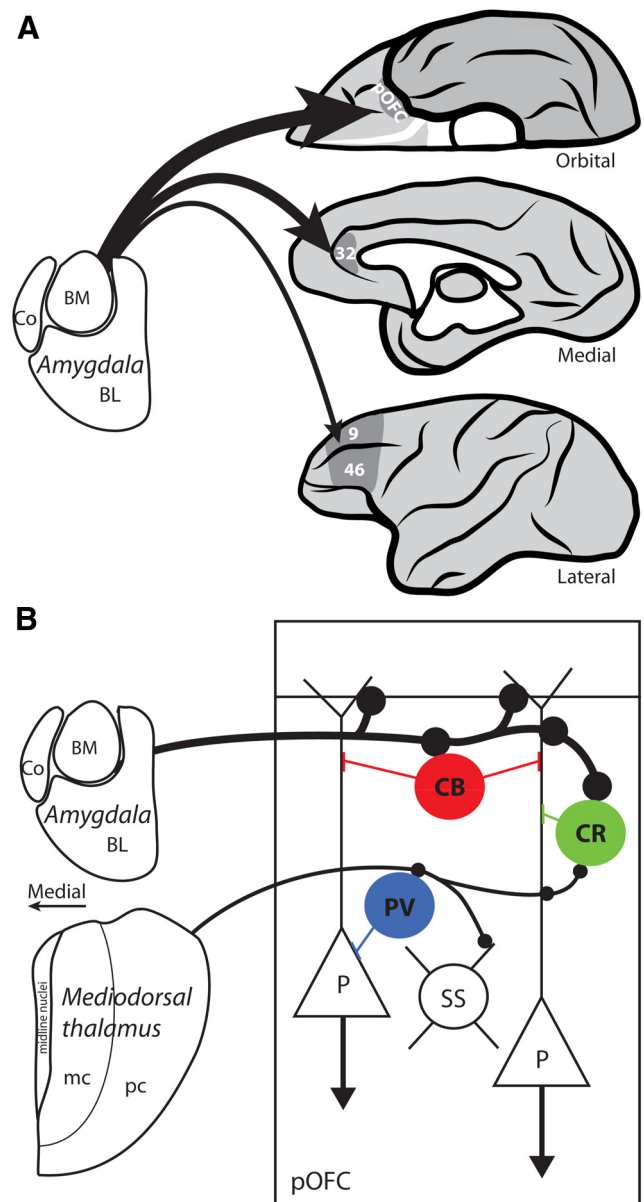


**Figure 7.** Summary of features in amygdalar pathway to pOFC, ACC, and areas 9/46. *A*, Thickness of arrows depicts the relative density and terminal size of amygdalar pathways to pOFC, ACC, and areas 9/46. *B*, Amygdalar terminals were larger and formed synapses more often with excitatory neurons in the upper layers compared with thalamic axons in the middle layers. Among inhibitory neurons, amygdalar axons targeted CB and CR neurons in the upper layers, while thalamic axons targeted more PV and CR neurons in the middle layers. Large amygdalar synapses may drive excitatory neurons in pOFC, while synapses on CB and CR neurons may reduce background excitation, or noise. Excitatory spiny stellate neurons (SS) are a major target of thalamic pathways. BL, Basolateral; BM, basomedial; Co, cortical; mc, magnocellular sector; P, pyramidal neuron; pc, parvicellular sector.

of task-specific stimuli, and quickly form associations related with reward and update them as conditions change (Tremblay and Schultz, 1999; Wallis and Miller, 2003; Simmons and Richmond, 2008; Morrison and Salzman, 2011; Luk and Wallis, 2013; Wilson et al., 2014). The above studies show that responses of neurons in orbitofrontal cortex vary based on task context, suggesting flexible integration of information. It has been hypothesized that processing flexibly the state of a task applies to diverse tasks that test function in orbitofrontal cortex across species (Wilson et al., 2014).

The ACC differs in several ways from the pOFC. While the pOFC is a stronger "receiver" of pathways from the amygdala, the ACC is a stronger "sender" of pathways to the amygdala (Ghashghaei et al., 2007). The emphasis in ACC appears to be in processing the value of actions and outcomes (Kennerley et al., 2006), consistent with its connections with cingulate motor areas (Barbas and Pandya, 1987; Morecraft and Van Hoesen, 1998). Further, the most robust projections of ACC are motor related and innervate brainstem and spinal autonomic centers (An et al., 1998; Rempel-Clower and Barbas, 1998; Barbas et al., 2003). These efferent autonomic pathways mediate emotional expression, including vocalizations and distress calls in primates (for review, see Vogt and Barbas, 1988; Devinsky et al., 1995; Hadland et al., 2003).

### Specialized amygdalar drivers to the upper layers of pOFC: comparison with the thalamic

The predominance of dense and potentially efficient pathways from the amygdala to the upper layers of pOFC is also unusual and different from thalamic relay pathways. In the latter, upper-layer terminations are thought to have a modulatory role (Sherman and Guillery, 1998). Dense pathways from thalamic relay nuclei target most densely the middle cortical layers (layers 3b–5a), a pattern seen also for MD to prefrontal cortex (Giguere and Goldman-Rakic, 1988). These thalamocortical pathways are described as drivers, capable of eliciting action potentials in postsynaptic neurons (Freund et al., 1989; Sommer and Wurtz, 2004). In contrast, amygdalar terminations in the upper layers were not only denser but also larger than the thalamic in the middle layers.

Synaptic specializations further suggest higher strength in the amygdalar pathway than the thalamic to pOFC. This is exemplified by amygdalar innervation of large spines, which are associated with large synapses and large EPSCs (Harris and Stevens, 1989; Matsuzaki et al., 2001). Multisynaptic amygdalar boutons were more frequent than the thalamic in pOFC; such boutons increase in number after long-term potentiation and learning (Jones et al., 1997; Muller et al., 2000; Geinisman et al., 2001). Finally, some amygdalar terminals formed perforated synapses, which are enriched with AMPA receptors and are thought to participate in more efficient computations (Geinisman, 2000; Nicholson et al., 2006; Nava et al., 2014).

The strong amygdalar pathway to the upper layers provides a circuit mechanism for extended influences in pOFC, by impinging on the apical dendrites and tufts of pyramidal neurons from layers 2, 3, and 5, as well as calbindin and calretinin inhibitory neurons (DeFelipe, 1997; Callaway, 1998; Douglas and Martin, 1998). The amygdalar pathway to the upper layers of pOFC may thus affect the activity of the entire cortical column, including neurons that project back to the amygdala, as shown in mouse medial prefrontal cortex (Little and Carter, 2013). In rhesus monkeys, neurons in layer 5 and to a lesser extent in layer 3 project to the amygdala (Ghashghaei et al., 2007), and pOFC uniquely targets the purely inhibitory intercalated masses (IMs) of the amygdala (Ghashghaei and Barbas, 2002). In turn, IM neurons project to the central amygdalar nucleus, a key output of the amygdala to brainstem and hypothalamic autonomic centers (for review, see Price, 2003; Barbas et al., 2011). The pOFC projects as well to the central nucleus, albeit to a lesser extent, and through these dual pathways the pOFC may flexibly adjust autonomic drive, depending on the circumstances (Ghashghaei and Barbas, 2002). When activated by the robust amygdalar pathways, the pOFC may modify the activity of the amygdala as conditions change (Simmons and Richmond, 2008), adding necessary flexibility in reward learning (John et al., 2013).

### Amygdalar drivers and feedforward inhibition: a mechanism for gain control

Like other long-distance pathways in primates, the amygdalar pathway to orbitofrontal cortex is excitatory (Miyashita et al., 2007). We found that the amygdala also innervates a higher proportion of excitatory postsynaptic sites than the thalamic, while the opposite applies for inhibitory postsynaptic targets. Among the small proportion of synapses with presumed inhibitory neurons, amygdalar axons innervated mostly CB and CR neurons in pOFC. CB neurons form synapses on distal dendrites of neighboring pyramidal neurons and mildly modulate them, while CR neurons modulate other inhibitory neurons in the upper layers (DeFelipe et al., 1989; DeFelipe, 1997). This circuit mechanism can enhance signal and reduce weak activity at the fringes of columns of neurons engaged in working memory tasks in monkey lateral prefrontal cortex (Constantinidis and Goldman-Rakic, 2002; Wang et al., 2004). By analogy, amygdalar axons may increase the signal-to-noise ratio by activating CB and CR inhibitory neurons and simultaneously drive neurons in pOFC through large and efficient synapses on excitatory postsynaptic targets (Fig. 7). This circuit mechanism may control gain by enhancing activation by relevant signals and reducing noise to help focus attention on stimuli with affective import. Interestingly, the amygdala, pOFC, and MD have in common robust and overlapping projections to the inhibitory thalamic reticular nucleus (TRN), which is thought to be the brain's vanguard for attention (for review, see Zikopoulos and Barbas, 2007a). All three pathways extend to the sensory sectors of TRN and may gate sensory stimuli with emotional significance (Zikopoulos and Barbas, 2012). The pathway to TRN provides an alternative route through which the amygdala may influence pOFC via the thalamic MD, to which it also projects (Russchen et al., 1987).

### Circuits for flexible behavior and their disruption in psychiatric diseases

Dynamic integration of external sensory stimuli and internal valuations in orbitofrontal cortex based on context (Simmons and Richmond, 2008; Wilson et al., 2014) is likely disrupted in a variety of psychiatric diseases, including obsessive–compulsive disorder (OCD) and phobias (Barbas et al., 2011; John et al., 2013). Specifically, pathways connecting the amygdala and orbitofrontal cortex have been implicated in the pathology of OCD, characterized by recurrent intrusive thoughts and impulses, leading to repetitive compulsive behaviors (for review, see Chamberlain et al., 2005; Maia et al., 2008; Arnsten and Rubia, 2012). OCD is thought to arise from excess activation of loops connecting the basal ganglia, the amygdala, ACC, and orbitofrontal cortex (Huey et al., 2008; Maia et al., 2008; Haber and Heilbronner, 2013). Specifically, the orbitofrontal cortex has reduced volume and shows increased activation in OCD patients experiencing symptoms (Breiter and Rauch, 1996; Szeszko et al., 1999; Adler et al., 2000; Kang et al., 2004). Lesions of the connections among orbitofrontal cortex, the thalamus, and basal ganglia have been used with some success as therapy for OCD (Maia et al., 2008; Greenberg et al., 2010). Further, the therapeutic effects of deep brain stimulation in a rat OCD model have been attributed to ultimate excitation of presumed inhibitory neurons and decreased firing rates of orbitofrontal neurons (McCracken and Grace, 2007).

The precise circuit neuropathology of OCD is not clearly understood. But based on the above studies, our findings suggest a

possible pathway mechanism, mediated through a strong excitatory amygdalar pathway to pOFC. Increased excitation from the amygdala in OCD may override the comparatively few synapses on the modulatory CB and CR neurons in pOFC, and compromise the ability to disambiguate the contextual significance of stimuli. Reduced inhibition in orbitofrontal cortex may decrease the ability to focus only on relevant stimuli and respond also to multiple other stimuli that richly impinge on pOFC.

# References

Adler CM, McDonough-Ryan P, Sax KW, Holland SK, Arndt S, Strakowski SM (2000) fMRI of neuronal activation with symptom provocation in unmedicated patients with obsessive compulsive disorder. J Psychiatr Res 34:317–324. CrossRef Medline

An X, Bandler R, Ongür D, Price JL (1998) Prefrontal cortical projections to longitudinal columns in the midbrain periaqueductal gray in macaque monkeys. J Comp Neurol 401:455–479. CrossRef Medline

Arnsten AF, Rubia K (2012) Neurobiological circuits regulating attention, cognitive control, motivation, and emotion: disruptions in neurodevelopmental psychiatric disorders. J Am Acad Child Adolesc Psychiatry 51: 356–367. CrossRef Medline

Bachevalier J, Loveland KA (2006) The orbitofrontal-amygdala circuit and self-regulation of social-emotional behavior in autism. Neurosci Biobehav Rev 30:97–117. CrossRef Medline

Barbas H (1997) Two prefrontal limbic systems: their common and unique features. In: The association cortex: structure and function (Sakata H, Mikami A, Fuster JM, eds), pp 99–115. Amsterdam: Harwood Academic.

Barbas H (2000) Connections underlying the synthesis of cognition, memory, and emotion in primate prefrontal cortices. Brain Res Bull 52:319–330. CrossRef Medline

Barbas H, De Olmos J (1990) Projections from the amygdala to basoventral and mediodorsal prefrontal regions in the rhesus monkey. J Comp Neurol 300:549–571. CrossRef Medline

Barbas H, Pandya DN (1987) Architecture and frontal cortical connections of the premotor cortex (area 6) in the rhesus monkey. J Comp Neurol 256:211–228. CrossRef Medline

Barbas H, Pandya DN (1989) Architecture and intrinsic connections of the prefrontal cortex in the rhesus monkey. J Comp Neurol 286:353–375. CrossRef Medline

Barbas H, Saha S, Rempel-Clower N, Ghashghaei T (2003) Serial pathways from primate prefrontal cortex to autonomic areas may influence emotional expression. BMC Neurosci 4:25. CrossRef Medline

Barbas H, Zikopoulos B, Timbie C (2011) Sensory pathways and emotional context for action in primate prefrontal cortex. Biol Psychiatry 69:1133–1139. CrossRef Medline

Bechara A, Damasio H, Damasio AR (2000) Emotion, decision making and the orbitofrontal cortex. Cereb Cortex 10:295–307. CrossRef Medline

Breiter HC, Rauch SL (1996) Functional MRI and the study of OCD: from symptom provocation to cognitive-behavioral probes of cortico-striatal systems and the amygdala. Neuroimage 4:S127–S138. CrossRef Medline

Callaway EM (1998) Local circuits in primary visual cortex of the macaque monkey. Annu Rev Neurosci 21:47–74. CrossRef Medline

Cavada C, Compañy T, Tejedor J, Cruz-Rizzolo RJ, Reinoso-Suárez F (2000) The anatomical connections of the macaque monkey orbitofrontal cortex. A review. Cereb Cortex 10:220–242. CrossRef Medline

Chamberlain SR, Blackwell AD, Fineberg NA, Robbins TW, Sahakian BJ (2005) The neuropsychology of obsessive compulsive disorder: the importance of failures in cognitive and behavioural inhibition as candidate endophenotypic markers. Neurosci Biobehav Rev 29:399–419. CrossRef Medline

Cohen J (1988) Statistical power analysis for the behavioral sciences. Hillsdale, NJ: Lawrence Erlbaum Associates.

Constantinidis C, Goldman-Rakic PS (2002) Correlated discharges among putative pyramidal neurons and interneurons in the primate prefrontal cortex. J Neurophysiol 88:3487–3497. CrossRef Medline

Cruikshank SJ, Ahmed OJ, Stevens TR, Patrick SL, Gonzalez AN, Elmaleh M, Connors BW (2012) Thalamic control of layer 1 circuits in prefrontal cortex. J Neurosci 32:17813–17823. CrossRef Medline

DeFelipe J (1997) Types of neurons, synaptic connections and chemical characteristics of cells immunoreactive for calbindin-D28K, parvalbumin and calretinin in the neocortex. J Chem Neuroanat 14:1–19. CrossRef Medline

DeFelipe J, Fariñas I (1992) The pyramidal neuron of the cerebral cortex:

morphological and chemical characteristics of the synaptic inputs. Prog Neurobiol 39:563–607. CrossRef Medline

DeFelipe J, Hendry SH, Jones EG (1989) Synapses of double bouquet cells in monkey cerebral cortex visualized by calbindin immunoreactivity. Brain Res 503:49–54. CrossRef Medline

Dermon CR, Barbas H (1994) Contralateral thalamic projections predominantly reach transitional cortices in the rhesus monkey. J Comp Neurol 344:508–531. CrossRef Medline

Devinsky O, Morrell MJ, Vogt BA (1995) Contributions of anterior cingulate cortex to behaviour. Brain 118:279–306. CrossRef Medline

Dombrowski SM, Hilgetag CC, Barbas H (2001) Quantitative architecture distinguishes prefrontal cortical systems in the rhesus monkey. Cereb Cortex 11:975–988. CrossRef Medline

Douglas RJ, Martin KA (1998) Neocortex. In: The synaptic organization of the brain, fourth edition (Shepherd GM, ed), pp 459–509. New York: Oxford UP.

Fiala JC (2005) Reconstruct: a free editor for serial section microscopy. J Microsc 218:52–61. CrossRef Medline

Freund TF, Martin KA, Soltesz I, Somogyi P, Whitteridge D (1989) Arborisation pattern and postsynaptic targets of physiologically identified thalamocortical afferents in striate cortex of the macaque monkey. J Comp Neurol 289:315–336. CrossRef Medline

Gabbott PL, Bacon SJ (1996) Local circuit neurons in the medial prefrontal cortex (areas 24a–c, 25 and 32) in the monkey: II. Quantitative areal and laminar distributions. J Comp Neurol 364:609–636. CrossRef Medline

Geinisman Y (2000) Structural synaptic modifications associated with hippocampal LTP and behavioral learning. Cereb Cortex 10:952–962. CrossRef Medline

Geinisman Y, Berry RW, Disterhoft JF, Power JM, Van der Zee EA (2001) Associative learning elicits the formation of multiple-synapse boutons. J Neurosci 21:5568–5573. Medline

Germuska M, Saha S, Fiala J, Barbas H (2006) Synaptic distinction of laminar specific prefrontal-temporal pathways in primates. Cereb Cortex 16: 865–875. Medline

Ghashghaei HT, Barbas H (2002) Pathways for emotions: interactions of prefrontal and anterior temporal pathways in the amygdala of the rhesus monkey. Neuroscience 115:1261–1279. CrossRef Medline

Ghashghaei HT, Hilgetag CC, Barbas H (2007) Sequence of information processing for emotions based on the anatomic dialogue between prefrontal cortex and amygdala. Neuroimage 34:905–923. CrossRef Medline

Giguere M, Goldman-Rakic PS (1988) Mediodorsal nucleus: areal, laminar, and tangential distribution of afferents and efferents in the frontal lobe of rhesus monkeys. J Comp Neurol 277:195–213. CrossRef Medline

Goldman-Rakic PS, Porrino LJ (1985) The primate mediodorsal (MD) nucleus and its projection to the frontal lobe. J Comp Neurol 242:535–560. CrossRef Medline

Greenberg BD, Rauch SL, Haber SN (2010) Invasive circuitry-based neurotherapeutics: stereotactic ablation and deep brain stimulation for OCD. Neuropsychopharmacology 35:317–336. CrossRef Medline

Haber SN, Heilbronner SR (2013) Translational research in OCD: circuitry and mechanisms. Neuropsychopharmacology 38:252–253. CrossRef Medline

Hadland KA, Rushworth MF, Gaffan D, Passingham RE (2003) The effect of cingulate lesions on social behaviour and emotion. Neuropsychologia 41:919–931. CrossRef Medline

Harris KM, Stevens JK (1989) Dendritic spines of CA 1 pyramidal cells in the rat hippocampus: serial electron microscopy with reference to their biophysical characteristics. J Neurosci 9:2982–2997. Medline

Huey ED, Zahn R, Krueger F, Moll J, Kapogiannis D, Wassermann EM, Grafman J (2008) A psychological and neuroanatomical model of obsessive-compulsive disorder. J Neuropsychiatry Clin Neurosci 20:390–408. CrossRef Medline

Jensen FE, Harris KM (1989) Preservation of neuronal ultrastructure in hippocampal slices using rapid microwave-enhanced fixation. J Neurosci Methods 29:217–230. CrossRef Medline

Jiao Y, Sun Z, Lee T, Fusco FR, Kimble TD, Meade CA, Cuthbertson S, Reiner A (1999) A simple and sensitive antigen retrieval method for freefloating and slide-mounted tissue sections. J Neurosci Methods 93:149–162. CrossRef Medline

John YJ, Bullock D, Zikopoulos B, Barbas H (2013) Anatomy and computational modeling of networks underlying cognitive-emotional interaction. Front Hum Neurosci 7:101. CrossRef Medline

Jones TA, Klintsova AY, Kilman VL, Sirevaag AM, Greenough WT (1997)

Induction of multiple synapses by experience in the visual cortex of adult rats. Neurobiol Learn Mem 68:13–20. CrossRef Medline

Kang DH, Kim JJ, Choi JS, Kim YI, Kim CW, Youn T, Han MH, Chang KH, Kwon JS (2004) Volumetric investigation of the frontal-subcortical circuitry in patients with obsessive-compulsive disorder. J Neuropsychiatry Clin Neurosci 16:342–349. CrossRef Medline

Kennerley SW, Walton ME, Behrens TE, Buckley MJ, Rushworth MF (2006) Optimal decision making and the anterior cingulate cortex. Nat Neurosci 9:940–947. CrossRef Medline

Little JP, Carter AG (2013) Synaptic mechanisms underlying strong reciprocal connectivity between the medial prefrontal cortex and basolateral amygdala. J Neurosci 33:15333–15342. CrossRef Medline

Luk CH, Wallis JD (2013) Choice coding in frontal cortex during stimulus-guided or action-guided decision-making. J Neurosci 33:1864–1871. CrossRef Medline

Maia TV, Cooney RE, Peterson BS (2008) The neural bases of obsessive-compulsive disorder in children and adults. Dev Psychopathol 20:1251–1283. CrossRef Medline

Matsuzaki M, Ellis-Davies GC, Nemoto T, Miyashita Y, Iino M, Kasai H (2001) Dendritic spine geometry is critical for AMPA receptor expression in hippocampal CA1 pyramidal neurons. Nat Neurosci 4:1086–1092. CrossRef Medline

McCracken CB, Grace AA (2007) High-frequency deep brain stimulation of the nucleus accumbens region suppresses neuronal activity and selectively modulates afferent drive in rat orbitofrontal cortex in vivo. J Neurosci 27:12601–12610. CrossRef Medline

McFarland NR, Haber SN (2002) Thalamic relay nuclei of the basal ganglia form both reciprocal and nonreciprocal cortical connections, linking multiple frontal cortical areas. J Neurosci 22:8117–8132. Medline

Medalla M, Barbas H (2012) The anterior cingulate cortex may enhance inhibition of lateral prefrontal cortex via m2 cholinergic receptors at dual synaptic sites. J Neurosci 32:15611–15625. CrossRef Medline

Medalla M, Lera P, Feinberg M, Barbas H (2007) Specificity in inhibitory systems associated with prefrontal pathways to temporal cortex in primates. Cereb Cortex 17 [Suppl 1]:i136–i150. Medline

Miller EK, Cohen JD (2001) An integrative theory of prefrontal cortex function. Annu Rev Neurosci 24:167–202. CrossRef Medline

Miyashita T, Ichinohe N, Rockland KS (2007) Differential modes of termination of amygdalothalamic and amygdalocortical projections in the monkey. J Comp Neurol 502:309–324. CrossRef Medline

Morecraft RJ, Van Hoesen GW (1998) Convergence of limbic input to the cingulate motor cortex in the rhesus monkey. Brain Res Bull 45:209–232. CrossRef Medline

Morrison SE, Salzman CD (2011) Representations of appetitive and aversive information in the primate orbitofrontal cortex. Ann N Y Acad Sci 1239:59–70. CrossRef Medline

Muller D, Toni N, Buchs PA (2000) Spine changes associated with long-term potentiation. Hippocampus 10:596–604. CrossRef Medline

Muly EC, Senyuz M, Khan ZU, Guo JD, Hazra R, Rainnie DG (2009) Distribution of D-1 and D-5 dopamine receptors in the primate and rat basolateral amygdala. Brain Struct Funct 213:375–393. CrossRef Medline

Murray EA (2007) The amygdala, reward and emotion. Trends Cogn Sci 11:489–497. CrossRef Medline

National Research Council (2011) Guide for the care and use of laboratory animals: eighth edition. Washington, DC: The National Academies.

Nava N, Chen F, Wegener G, Popoli M, Nyengaard JR (2014) A new efficient method for synaptic vesicle quantification reveals differences between medial prefrontal cortex perforated and nonperforated synapses. J Comp Neurol 522:284–297. CrossRef Medline

Nicholson DA, Trana R, Katz Y, Kath WL, Spruston N, Geinisman Y (2006) Distance-dependent differences in synapse number and AMPA receptor expression in hippocampal CA1 pyramidal neurons. Neuron 50:431–442. CrossRef Medline

Ostroff LE, Cain CK, Bedont J, Monfils MH, Ledoux JE (2010) Fear and safety learning differentially affect synapse size and dendritic translation

in the lateral amygdala. Proc Natl Acad Sci U S A 107:9418–9423. CrossRef Medline

Peters A, Kaiserman-Abramof IR (1969) The small pyramidal neuron of the rat cerebral cortex. The synapses upon dendritic spines. Z Zellforsch Mikrosk Anat 100:487–506. CrossRef Medline

Peters A, Palay SL, Webster HD (1991) The fine structure of the nervous system. Neurons and their supporting cells. New York: Oxford UP.

Porrino LJ, Crane AM, Goldman-Rakic PS (1981) Direct and indirect pathways from the amygdala to the frontal lobe in rhesus monkeys. J Comp Neurol 198:121–136. CrossRef Medline

Price JL (2003) Comparative aspects of amygdala connectivity. Ann N Y Acad Sci 985:50–58.

Reichova I, Sherman SM (2004) Somatosensory corticothalamic projections: distinguishing drivers from modulators. J Neurophysiol 92:2185–2197. CrossRef Medline

Rempel-Clower NL, Barbas H (1998) Topographic organization of connections between the hypothalamus and prefrontal cortex in the rhesus monkey. J Comp Neurol 398:393–419. CrossRef Medline

Rosene DL, Roy NJ, Davis BJ (1986) A cryoprotection method that facilitates cutting frozen sections of whole monkey brains from histological and histochemical processing without freezing artifact. J Histochem Cytochem 34:1301–1315. CrossRef Medline

Russchen FT, Amaral DG, Price JL (1987) The afferent input to the magnocellular division of the mediodorsal thalamic nucleus in the monkey, Macaca fascicularis. J Comp Neurol 256:175–210. CrossRef Medline

Shelton L, Becerra L, Borsook D (2012) Unmasking the mysteries of the habenula in pain and analgesia. Prog Neurobiol 96:208–219. CrossRef Medline

Sherman SM, Guillery RW (1998) On the actions that one nerve cell can have on another: distinguishing "drivers" from "modulators." Proc Natl Acad Sci U S A 95:7121–7126. CrossRef Medline

Simmons JM, Richmond BJ (2008) Dynamic changes in representations of preceding and upcoming reward in monkey orbitofrontal cortex. Cereb Cortex 18:93–103. CrossRef Medline

Sommer MA, Wurtz RH (2004) What the brain stem tells the frontal cortex. I. Oculomotor signals sent from superior colliculus to frontal eye field via mediodorsal thalamus. J Neurophysiol 91:1381–1402. Medline

Szeszko PR, Robinson D, Alvir JM, Bilder RM, Lencz T, Ashtari M, Wu H, Bogerts B (1999) Orbital frontal and amygdala volume reductions in obsessive-compulsive disorder. Arch Gen Psychiatry 56:913–919. CrossRef Medline

Tremblay L, Schultz W (1999) Relative reward preference in primate orbitofrontal cortex. Nature 398:704–708. CrossRef Medline

Vogt BA, Barbas H (1988) Structure and connections of the cingulate vocalization region in the rhesus monkey. In: The physiological control of mammalian vocalization (Newman JD, ed), pp 203–225. New York: Plenum.

Wallis JD, Miller EK (2003) Neuronal activity in primate dorsolateral and orbital prefrontal cortex during performance of a reward preference task. Eur J Neurosci 18:2069–2081. CrossRef Medline

Wallis JD, Dias R, Robbins TW, Roberts AC (2001) Dissociable contributions of the orbitofrontal and lateral prefrontal cortex of the marmoset to performance on a detour reaching task. Eur J Neurosci 13:1797–1808. CrossRef Medline

Wang XJ, Tegnér J, Constantinidis C, Goldman-Rakic PS (2004) Division of labor among distinct subtypes of inhibitory neurons in a cortical microcircuit of working memory. Proc Natl Acad Sci U S A 101:1368–1373. CrossRef Medline

Wilson RC, Takahashi YK, Schoenbaum G, Niv Y (2014) Orbitofrontal cortex as a cognitive map of task space. Neuron 81:267–279. CrossRef Medline

Zikopoulos B, Barbas H (2007a) Circuits for multisensory integration and attentional modulation through the prefrontal cortex and the thalamic reticular nucleus in primates. Rev Neurosci 18:417–438. Medline

Zikopoulos B, Barbas H (2007b) Parallel driving and modulatory pathways link the prefrontal cortex and thalamus. PLoS One 2:e848. CrossRef Medline

Zikopoulos B, Barbas H (2012) Pathways for emotions and attention converge on the thalamic reticular nucleus in primates. J Neurosci 32:5338–5350. CrossRef Medline